

# Study of monolithic CMOS pixel sensors in the Belle II experiment upgrade

October 19, 2023

# Contents

<b>1 Belle II and SuperKEKB (SKB) accelerator</b>	<b>4</b>
1.1 Physics program of the B-factories . . . . .	4
1.1.1 Open questions in SM . . . . .	5
1.1.2 Peculiarity of asymmetric B factories . . . . .	5
1.2 SuperKEKB accelerator . . . . .	7
1.2.1 The facility . . . . .	7
1.2.2 "Nano-beam" scheme . . . . .	8
1.3 Belle II detector . . . . .	9
1.3.1 Vertex Detectors (VXD) . . . . .	9
1.3.2 Central Drift Chamber (CDC) . . . . .	10
1.3.3 Particle identification system (TOP e ARICH) . . . . .	11
1.3.4 Electromagnetic calorimeter (ECL) . . . . .	13
1.3.5 $K_L$ muon detector (KLM) . . . . .	13
1.3.6 Trigger system . . . . .	13
1.4 Current state of data taking . . . . .	14
<b>2 Belle II Upgrade</b>	<b>16</b>
2.1 Background sources and limitations in Belle II . . . . .	16
2.1.1 Major background sources . . . . .	16
2.1.2 Current background status and future predictions . . . . .	17
2.2 Purposes of the upgrade . . . . .	19

2.3	Summary of possible VXD upgrade . . . . .	20
2.3.1	Depleted Field Effect Transistor (DEPFET) . . . . .	20
2.3.2	Thin and Fine-Pitch SVD . . . . .	21
2.3.3	Silicon On Insulator (SOI) . . . . .	21
2.3.4	CMOS Monolithic Active Pixels Sensor . . . . .	23
<b>3</b>	<b>VTX detector</b>	<b>26</b>
3.1	VTX Layout and mechanical structure . . . . .	26
3.1.1	iVTX . . . . .	27
3.1.2	oVTX . . . . .	29
3.1.3	Thermomechanics and data transmission . . . . .	31
3.2	Performance simulation . . . . .	32
3.2.1	Potential VTX geometries . . . . .	32
3.2.2	Tracking efficiency at low momentum and impact parameter resolution . . . . .	32
3.2.3	Vertexing resolution . . . . .	34
3.3	OBELIX chip design . . . . .	36
3.3.1	Sensor specification . . . . .	36
3.3.2	Sensor implementation . . . . .	37
<b>4</b>	<b>Conclusions</b>	<b>40</b>

# 1. Belle II and SuperKEKB (SKB) accelerator

The first chapter introduces some of the main unexplained aspects of the Standard Model (SM), on which the Belle II physics program is founded. A short description of the SuperKEKB accelerator and the Belle II detector's structure is also presented and in conclusion some highlights on the current state of measurements.

## 1.1 Physics program of the B-factories

The SM is a physics theory that describes three of the fundamental forces involving elementary particles, which are strong, weak and electromagnetic interaction (with the exclusion of the gravitational one). It classifies all the elementary constituents of matter in 4 main groups: quark, leptons, bosons and Higgs, as shown in Figure 1.1.



Figure 1.1: Particle classification in the Standard Model.

### 1.1.1 Open questions in SM

Despite the undeniable success of the SM in making predictions on physical phenomena, which have been experimentally verified with high precision over the years, there are many aspects of the Nature on which it is unable to give answers. Some of them are listed in the following.

- Three generations of quark and leptons have been discovered, but it is not known whether they should be the only ones and the reasons behind their mass hierarchy.
- Higgs mechanism is able to explain the cause of elementary particles' masses through spontaneous electro-weak symmetry breaking, but it is not clear whether neutrinos could gain their masses through the interaction with the Higgs boson.
- Another open question is the matter-antimatter asymmetry in the Universe. Even though Charge-Parity (CP) violation is necessary to explain its current state, the observed quantity is several orders of magnitude less than needed to explain the matter domination over antimatter, which allowed the evolution of the universe as we know it today.
- In the SM the Cabibbo-Kobayashi-Maskawa (CKM) matrix describes the flavour-changing weak interaction through the mismatch between the quantum state of the freely propagating quarks. It could be parametrized by three mixing angles and a complex phase that is at the foundation of CP violation in the quark flavor sector. The fact that its elements are almost diagonal might suggest the existence of a new symmetry, that is unbroken at high energy (greater than the order of TeV).
- Several astrophysical observations have been postulated the existence of dark matter, but its origin and nature have not been explained yet.

All these topics encourage the research of new particles and processes that could give reasonable answers.

At the energy frontier, experiments like the Large Hadron Collider (LHC) in Geneva are looking for new particles created from the proton-proton collision with a center mass energy up to 14 TeV.

At luminosity frontier instead, the hint of new particles and mechanisms is searched in precision measurements of suppressed reactions in flavour physics or in the deviations from SM. The discrepancies indeed, could be interpreted as a clue of new physics beyond SM. The last is the Belle II approach.

In particular the experiment investigates the CP violation in the B mesons system and it also searches for new physics evidences in the decays of B and D mesons, in  $\tau$  leptons and in the dark matter sector (DM).

### 1.1.2 Peculiarity of asymmetric B factories

The center of mass energy of Belle II experiment has its peak at the  $\Upsilon(4S)$  resonance, such as  $\sqrt{s} = 10.58$  GeV, which decays almost instantaneously into two B mesons ( $B^0 - \bar{B}^0$ ) in nearly 96% of all cases.

The main task of the VerteX Detector (VXD) is to reconstruct the production and decay vertices of the particles originated from the beam collisions. This aspect is crucial to perform time-dependent measurements, core of the Belle II physics program.

The choice of the asymmetric configuration of the beams relies precisely in the requirement to boost the mesons in order to measure their life-time, exploiting the information on the distance between their decay vertices. In fact in a beam symmetric situation, they would have been produced at rest, decaying roughly at the same point or in any case at undetectable distances. The investigation of CP violating processes instead, requires to measure the decay time difference of the two B mesons and its uncertainty is dominated by that of the decay vertex measurement (order of hundreds microns). Let us look at this in more details.

SuperKEKB collides an electrons beam of 7 GeV (High Energy Ring, HER) with a positrons beam of 4 GeV (Low Energy Ring, LER) and for this configuration results a Lorentz boost factor of the  $\Upsilon(4S)$  of  $(\beta\gamma)_{\Upsilon(4S)} \approx 0.28$ .

The same boost is also acquired by B mesons, because they are produced almost at rest ( $m_{\Upsilon(4S)} - m_{B^0} \approx 19$  MeV). Moreover knowing that  $\tau_B \simeq 1.5 \times 10^{-12}$  s and so  $c\tau_B \simeq 450 \mu\text{m}$ , we can compute the average flight distance travelled before decaying:

$$l = (\beta\gamma)_{\Upsilon(4S)} c\tau_B \approx 126 \mu\text{m} \quad (1.1)$$

This value must be within the vertex detector sensitivity in order to distinguish the vertex decay and as consequence to make precision measurements of lifetimes, mixing parameters and CP violation. The six-layer VXD could determines the position of the vertices with a precision better than  $100 \mu\text{m}$ , allowing to reconstruct secondary vertices, i.e. the decay position of the particles coming from B decays, and also from  $\tau$  leptons and D mesons.

We want to take a closer look at the event kinematics (e.g. Figure 1.2). The two B mesons are produced in an entangled quantum state, so from the decay products of the first it is possible to assign its flavor (for example  $B^0$ , identified as  $B_{tag}^0$ ) and accordingly that of the second, which will be the opposite ( $\bar{B}^0$ , called  $\bar{B}_{phys}^0$ ).

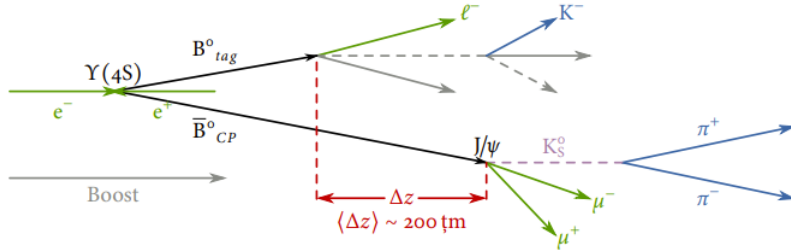


Figure 1.2: Example of the kinematics of the golden channel of Belle II experiment.

After this reconstruction, both B decay vertex positions in the longitudinal direction  $z_1$  and  $z_2$  are evaluated, in order to compute their difference:

$$\Delta z = z_1 - z_2 = (\beta\gamma)_{\Upsilon(4S)} c \Delta t \quad (1.2)$$

where  $\Delta t$  is the proper time decay difference. Another important parameter used in the reconstruction is  $d_0$ , which is the B decay vertex position from the primary vertex in the transverse plane.

Therefore this topology allows to transform a temporal information in a spatial one that we are able to measure. Without the boosted center of mass none of it could be possible, and this is an essential feature for an asymmetric B-factory.

## 1.2 SuperKEKB accelerator

Belle II sensitivity in the precision measurements is feasible especially thanks to the extraordinary performance of the SuperKEKB accelerator which host the (almost) hermetic detector. This complex facility is the result of efforts and efficient collaboration between the researches of KEK laboratory and all the international working groups that partecipate to the experiment.

### 1.2.1 The facility

SuperKEKB (Figure 1.3) is an asymmetric  $e^+e^-$  collider with a circumference of 3 km and a center of mass energy peak equal to  $\sqrt{s} = 10.58$  GeV, which corresponds to the mass of the  $\Upsilon(4S)$  resonance. Compared to its predecessor KEKB (which started its operation in 1998 and concluded it in 2010), the current accelerator has allowed to obtain the highest luminosity ever achieved, equal to  $4.7 \times 10^{34} \text{ cm}^{-2}\text{s}^{-1}$  in July 2022. This target was possible using a new scheme to accelerate and collide the beams, the so called *nano-beam scheme* (subsection 1.2.2).

Furthermore a new upgrade of the machine, still under study, will also include other interventions especially to cope with higher background levels, in view of a future increase in luminosity.

#### Luminosity

Istantaneous luminosity is one of the key parameters of any accelerator and it represents the interaction rate per unit of cross section between colliding particles. Reversing this equation is possible to obtain N, namely the number of the physical events produced in the interaction with a given luminosity:

$$L = \frac{1}{\sigma} \frac{dN}{dt} \quad \Rightarrow \quad N = \int_0^T L \sigma dt \quad (1.3)$$

where T is the duration of the experiment,  $\sigma$  the cross section of the physical process of interest. Although this is a raw information, as it does not consider other important factors that could influence the effective number of events produced, it becomes a significant starting point when one wants to study very rare processes such as Belle II. Specifically luminosity is strictly dependent from both machine and beam parameters. With respect to this, it can be expressed as:

$$L = \frac{\gamma_\pm}{2er_e} \left(1 + \frac{\sigma_y^*}{\sigma_x^*}\right) \left(\frac{I_\pm \xi_{y\pm}}{\beta_y^*}\right) \left(\frac{R_L}{R_{\xi_{y\pm}}}\right) \quad (1.4)$$

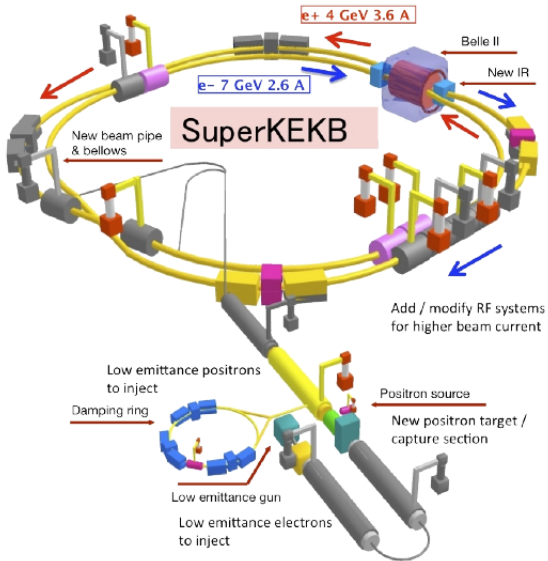


Figure 1.3: SuperKEKB accelerator structure.

where "±" denotes respectively positrons and electrons beam,  $\sigma_{x,y}^*$  is the beam size at the Interaction Point (IP) in the horizontal and vertical plane,  $I$  is the beam current,  $\beta_y^*$  the vertical beta function at the IP.  $\xi_{y\pm}$  is the vertical beam parameter which include the horizontal beta function at the IP, the horizontal emittance, the bunch length and the crossing angle between the beams.  $R_L$  and  $R_{\xi_{y\pm}}$  are the reduction factors due to geometrical loss such as the hour-glass effect and finite crossing.

As already mentioned, SuperKEKB holds the actual world record in luminosity (with  $\beta_y^* = 1.0$  mm) and in the near future the target will be to reach  $6 \times 10^{35} \text{ cm}^{-2}\text{s}^{-1}$  (by the 2030s), by increasing current beams and reducing their section at the IP, through the decrease of the betatron function down to  $\beta_y^* = 0.3$  mm. But this process makes the beam-induced background grow a lot, risking deterioration and poor functioning of the detectors.

For these reasons the supervision of the beams background becomes crucial: right now it has been estimated that the background should remain acceptable up to a luminosity value equal to  $2.8 \times 10^{35} \text{ cm}^{-2}\text{s}^{-1}$  with  $\beta_y^* = 0.6$  mm. So the chance to achieve higher luminosity is closely related to an upgrade plan of both the whole detector and the accelerator.

### 1.2.2 "Nano-beam" scheme

We have seen that the *beta function*  $\beta$  at the IP ( $\beta^*$ ) is a decisive factor to define the luminosity. To be able to ramp the luminosity up, it is necessary to reduce the value of  $\beta$  depending also, but not only, on the variation of the other machine parameters that appear in the Equation 1.4.

The mechanism used in SuperKEKB is called *nano-beam scheme*, and it allowed to obtain luminosity 40 times greater than that of KEKB, managing to

decrease of 1/20 the  $\beta^*$ .

This new scheme, originally designed by P. Raimondi, dictates that the beam bunches have to collide with sufficiently small  $\sigma_x^*$  and at large angle. In case of SuperKEKB the latter is equal to 83 mrad at the IP (larger with respect to the crossing angle used in KEKB) with the beam size of 50 nm in the vertical direction and 100  $\mu\text{m}$  in the horizontal direction (in Figure 1.4 a simplified representation of the differences).

This strategy also helps to reduce the *hourglass effect*, which happens when the  $\beta^*$  is comparable or smaller than the bunch length, causing a decrease in luminosity. As a matter of fact with larger crossing angle at the IP, the overlap length which is the effective bunch length, is much shorter than the bunch length along the beam axis.

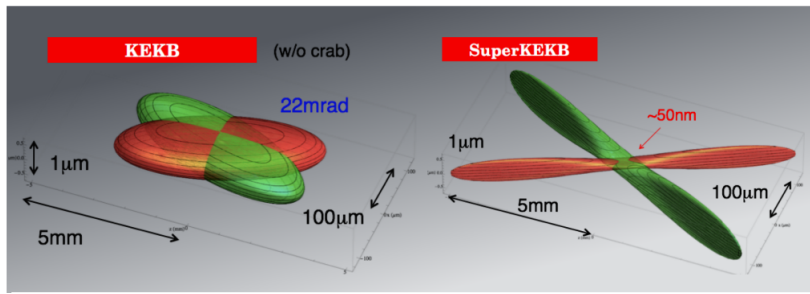


Figure 1.4: Comparison between the beam schemes used in KEKB and SuperKEKB.

Using a crossing angle large enough has other positive implications on the operation of the accelerator and its further improvements, like allowing the placement of a new focusing system at the IP (which may require more space), considering a future redesign of the interaction region.

### 1.3 Belle II detector

The Belle II detector is a general-purpose spectrometer which consists of a nested subdetectors sequence placed around the berillium beam pipe of 10 mm radius, nearby the IP of the two beams. Here we will go through a briefly description of the several subdetectors (Figure 1.5) going in order from the beam pipe outwards: the Vertex Detectors, the Central Drift Chamber, the TOP and the ARICH, the electromagnetic calorimeter and the  $K_L$  muon detector.

#### 1.3.1 Vertex Detectors (VXD)

The **VerteX Detector (VXD)** is composed by two devices divided into layers, the silicon Pixel Detector (PXD) and the Silicon Vertex Detector (SVD), for a total of six layers around the beam pipe.

The inner two layers of PXD (L12) consist of pixelated sensors based on the depleted field effect transistor (DEPFET) technology, realised with very thin (<

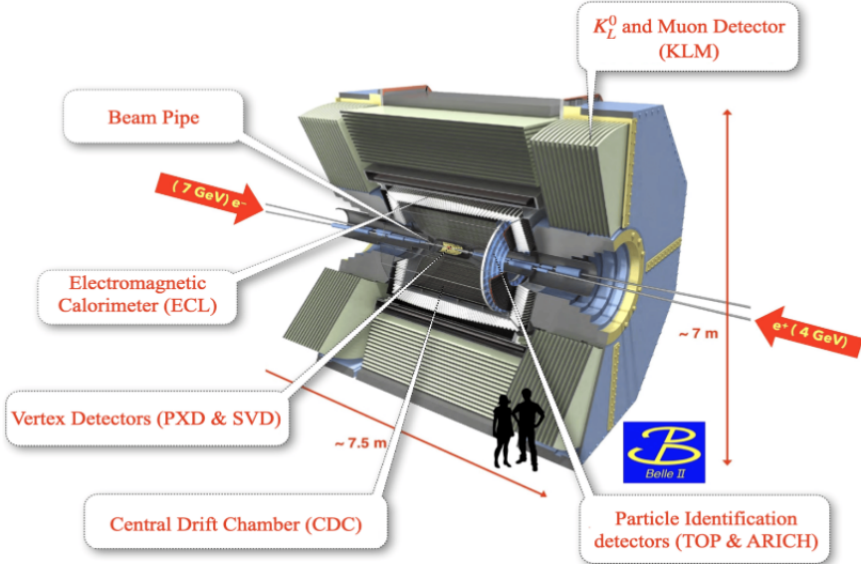


Figure 1.5: Belle II detector.

$100 \mu\text{m}$ ) sensors which allows to minimise multiple scattering, thus improving the tracking resolution for low-momentum particles. They are at a radius of 14 mm and 22 mm, respectively.

The remaining four layers of SVD (L3456) instead, are equipped with double-sided silicon strip (DSSD) sensors (at 39 mm, 80 mm, 104 mm and 135 mm respectively). Since a lower background rate is expected with respect to PXD, DSSD allow to achieve similar performance with a much smaller number of readout channels. These layers are mainly used for tracking/vertexing and also for particle identification (PID), through the measurement of the energy loss ( $dE/dx$ ).

We can notice in Figure 1.6 that because of the essential asymmetric configuration of the beam energies and the consequent boost of the particles produced in the collisions (subsection 1.1.2), the structure of the vertex detectors is also asymmetric along the longitudinal axis.

### 1.3.2 Central Drift Chamber (CDC)

This is the central tracking device, with a large-volume drift chamber and small drift cells. The chamber gas is composed of a He–C<sub>2</sub>H<sub>6</sub> (50:50) mixture with an average drift velocity of  $3.3 \text{ cm } \mu\text{s}^{-1}$  and a maximum drift time of about 350 ns for a 17 mm cell size.

The CDC contains 14336 wires arranged in 56 layers either in *axial* (aligned with the solenoidal magnetic field) or *stereo* (skewed with respect to the axial wires) orientation (Figure 1.7). In fact by combining information from both the axial and the stereo layers it is possible to reconstruct full three-dimensional helix charged tracks and measure their momenta. It also provides information for PID by measuring ionization energy loss, which is particularly useful for low-

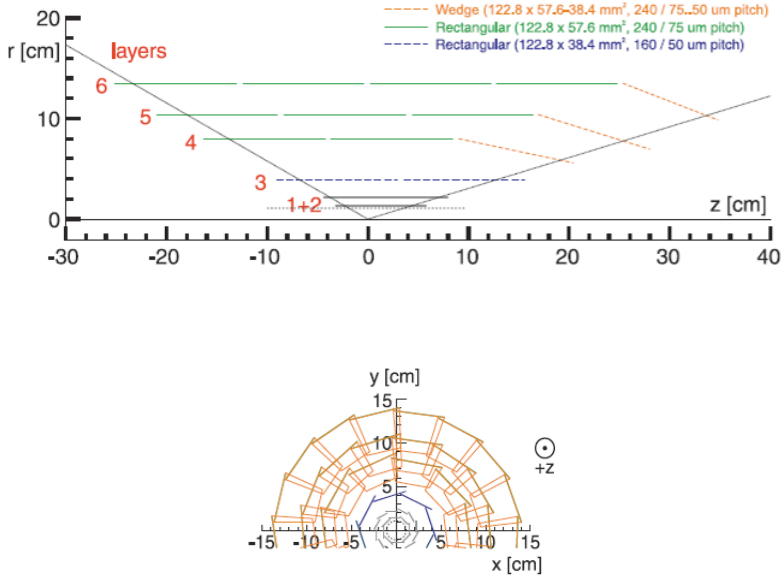


Figure 1.6: A schematic view of the Belle II vertex detector with a Be beam pipe and the six layers of PXD and SVD.

momentum particles that cannot reach the outer subdetectors dedicated also to deal with PID.

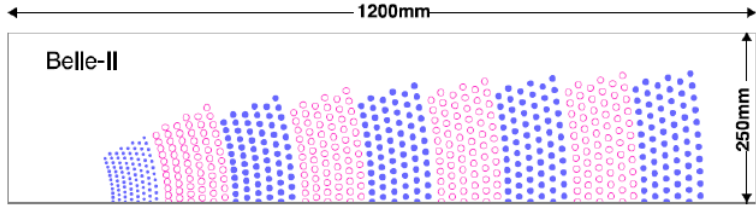


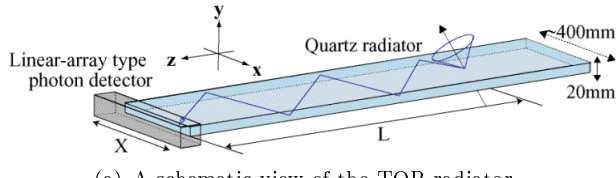
Figure 1.7: Schematic view of the CDC drift cells: blue dots represent the axial wires and the pink empty ones the stereo wires.

### 1.3.3 Particle identification system (TOP e ARICH)

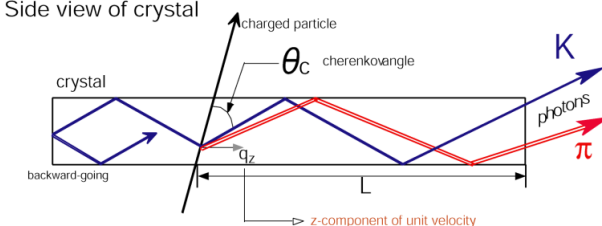
**TOP (Time Of Propagation)** is a special kind of Cherenkov detector used for PID in the barrel region. It employs the two-dimensional information of a Cherenkov ring image, such as the time of arrival and the impact position of Cherenkov photons at the photodetector at one end of a 2.6 m quartz bar. It is composed by 16 detector modules, each one consisted in a  $45 \times 2$  cm quartz bar (Cherenkov radiator) with a small expansion volume (about 10 cm long) at the sensor end of the bar (Figure 1.8).

In order to achieve a single-photon time resolution of about 100 ps (required for a good PID), 16-channel of microchannel plate photomultiplier tubes (MCP-

PMT) are employed, specially developed for this purpose.



(a) A schematic view of the TOP radiator.



(b) A side view of the TOP radiator.

Figure 1.8: TOP detector.

**ARICH (Aerogel Ring Imaging CHerenkov)** is used to identify charged particles and it is placed in the forward endcap region. It is a proximity focusing Cherenkov ring-imaging detector which adopts aerogel as Cherenkov radiator. In particular this detector employs a novel method to increase the number of detected Cherenkov photons: two 2 cm-thick layers of aerogel with different refractive indices ( $n_1 = 1.045$  upstream,  $n_2 = 1.055$  downstream) that increase the yield without degrading the Cherenkov angle resolution (Figure 1.9).

A hybrid avalanche photon detector (HAPD) are exploited as single-photon-sensitive high-granularity sensor. Here photo-electrons are accelerated over a potential difference of about 8 KV and are detected in avalanches photodiodes (APD).

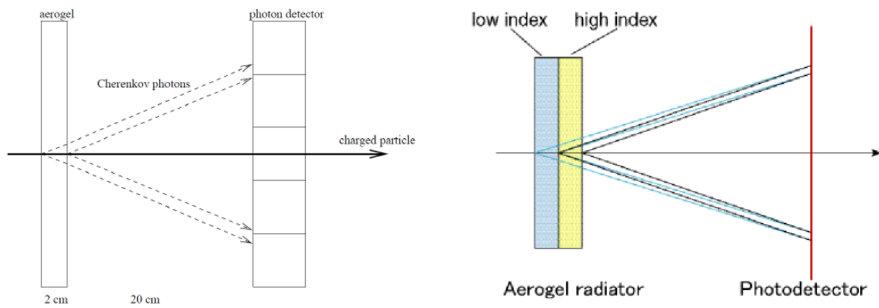


Figure 1.9: ARICH detector.

The main task of these detectors is to improve the  $K/\pi$  separation until 3.5 and 4 GeV/c of momentum, respectively.

### 1.3.4 Electromagnetic calorimeter (ECL)

The **ECL** is a highly segmented array of tellium-doped caesium iodide CsI(Tl) crystals assembled in a 3 m long barrel section with a radius of 1.25m, and two endcaps discs located at 2 m (forward) and 1 m (backward). All of them are instrumented with a total of 8736 crystal, covering about 90% of the solid angle in center-of-mass system.

This detector is used to detect gamma rays and to identify electrons in order to separate the latter from hadrons, especially pions.

### 1.3.5 $K_L$ muon detector (KLM)

It consists of an alternating sandwich of 4.7 cm-thick iron plates and active detector elements located outside the volume of the superconducting solenoid that provides a 1.5 T magnetic field. The iron plates serve as the magnetic flux return joke for the solenoid. They also provide 3.9 interaction lengths or more of material, beyond the 0.8 interaction lengths of the calorimeter in which  $K_L^0$  mesons can shower hadronically. The active detector elements have been chosen in order to cope with the reduction of the detector efficiency under the SuperKEKB background rates: resistive plate chambers (RPCs) for the outermost active layers and in the two innermost layers of the barrel and endcaps regions, scintillator strips with wavelength-shifting fibers are used, readout by silicon photomultipliers (SiPMs).

In Figure 1.10 a summary of the main characteristics of all subdetectors.

Purpose	Name	Component	Configuration	Readout channels	$\theta$ coverage
Beam pipe	Beryllium		Cylindrical, inner radius 10 mm, 10 $\mu\text{m}$ Au, 0.6 mm Be, 1 mm paraffin, 0.4 mm Be		
Tracking	PXD	Silicon pixel (DEPFET)	Sensor size: $15 \times (L1\ 136, L2\ 170)\text{mm}^2$ , pixel size: $50 \times (L1a\ 50, L1b\ 60, L2a\ 75, L2b\ 85)\mu\text{m}^2$ ; two layers at radii: 14, 22 mm	10M	[17°; 150°]
	SVD	Silicon strip	Rectangular and trapezoidal, strip pitch: 50(p)/160(n)–75(p)/240(n) $\mu\text{m}$ , with one floating intermediate strip, four layers at radii: 39, 80, 104, 135 mm	224k	[17°; 150°]
	CDC	Drift chamber with He-C <sub>2</sub> H <sub>6</sub> gas	14 336 wires in 56 layers, inner radius 160 mm, outer radius 1130 mm	14k	[17°; 150°]
Particle ID	TOP	RICH with quartz radiator	16 segments in $\phi$ at $r \approx 120$ cm, 275 cm long, 2 cm-thick quartz bars with 4 × 4-channel MCP PMTs	8k	[31°; 128°]
	ARICH	RICH with aerogel radiator	2 × 2 cm-thick focusing radiators with different $n$ , HAPD photodetectors	78k	[14°; 30°]
Calorimetry	ECL	CsI(Tl)	Barrel: $r = 125$ –162 cm, endcap: $z = -102$ –+196 cm	6624 (barrel), 1152 (FWD), 960 (BWD)	[12.4°; 31.4°], [32.2°; 128.7°], [130.7°; 155.1°]
Muon ID	KLM	barrel: RPCs and scintillator strips	2 layers with scintillator strips and 12 layers with 2 RPCs	$\theta$ 16k, $\phi$ 16k	[40°; 129°]
	KLM	endcap: scintillator strips	12 layers of $(7$ – $10) \times 40\text{ mm}^2$ strips	17k	[25°; 40°], [129°; 155°]

Figure 1.10: Summary of the main characteristics of all subdetectors.

### 1.3.6 Trigger system

The trigger system of Belle II has a non-trivial role to identify events of interest during data-taking at SuperKEKB, where high background rates are expected.

This system is divided into two levels: a hardware-based low-level trigger (L1) and a software-based high-level trigger (HLT), implemented in the data acquisition (DAQ) system.

- **L1**: has a latency of  $5 \mu\text{s}$  and a maximum trigger output rate of 30 kHz, limited by the read-in rate of the DAQ.
- **HLT**: is a key component of the DAQ, used to fully reconstruct events that pass the L1 trigger selection. It has to reduce online event rates to 10 kHz for offline storage and it must identify track regions of interest for PXD readout in order to reduce data flux. It fully recreates events with offline reconstruction algorithms, using all detectors information except for the PXD.

## 1.4 Current state of data taking

SuperKEKB accelerator reaches a new luminosity peak of  $4.7 \times 10^{34} \text{ cm}^{-2}\text{s}^{-1}$  in July 2022 (Figure 1.11).

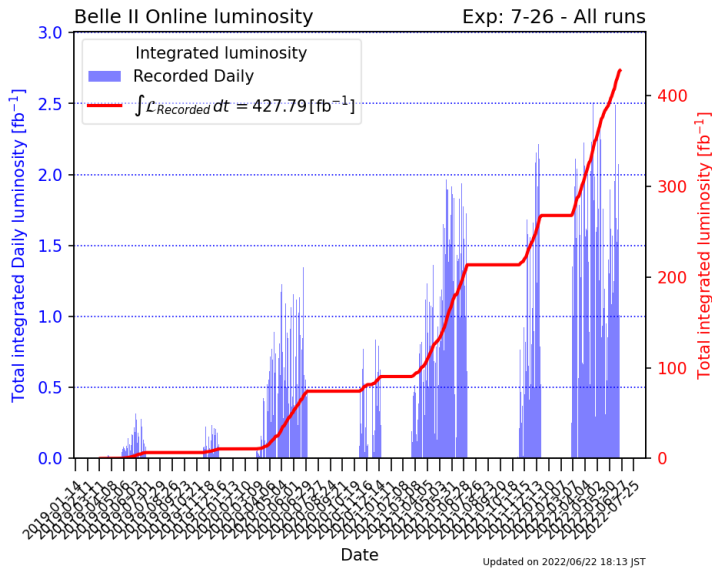


Figure 1.11: Total recorded integrated luminosity before Long Shutdown 1.

In further perspectives, the target of SuperKEKB is to achieve a new record with  $L_{ist} = 6 \times 10^{35} \text{ cm}^{-2}\text{s}^{-1}$  and to increase the integrated luminosity from  $428 \text{ fb}^{-1}$  (current value, starting in 2019) to  $50 \text{ fb}^{-1}$  (projection plot shown in Figure 1.12), in order to increase the statistics and as consequence the hope to give an insight in some of the questions still open in the SM.

To accomplish the fixed goals mentioned above, an upgrade not only of the vertex detector but also of the whole experiment and of the interaction region is necessary, among several reasons, to cope with a more complex circumstances due to the increased luminosity which undermine its proper functioning.

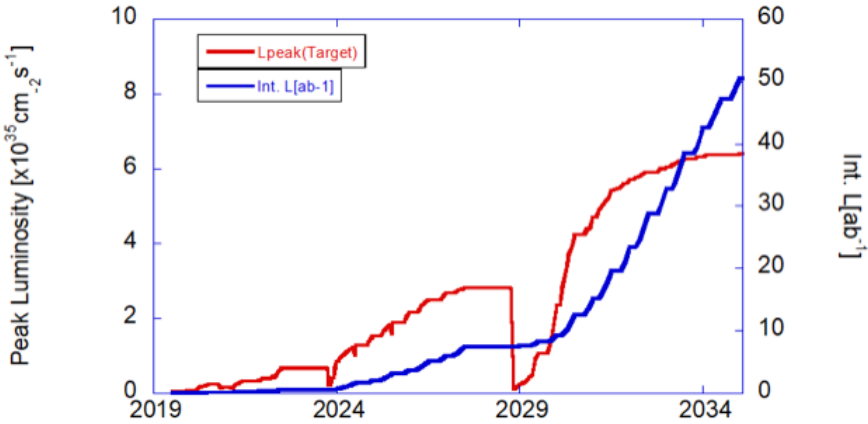


Figure 1.12: Luminosity projection plot (plan for the coming years).

Therefore a three-phase program has been drawn up:

- **short term:** year 2022. Long Shutdown 1 (LS1) is planned for approximately 15 months starting in July 2022, in order to install a complete pixel detector (PXD).
- **medium term:** approximately year 2028-29. Long Shutdown 2 (LS2) will probably be needed for the upgrade of the Interaction Region (IR) to reach a new luminosity target  $L_{peak} = 6 \times 10^{35} \text{ cm}^{-2} \text{s}^{-1}$ . Several open questions and difficulties have triggered many studies and discussions about a possible redesign of the machine lattice during this phase. In particular it would be necessary to deal with the limitation of the optics of the machine, concerning the further increasing of the luminosity and accordingly of the backgrounds rates. A new Vertex Detector might be also required, to accommodate the new IR design, and other sub-detector upgrades are possible.
- **long term:** years  $> 2032$ . Studies have started to explore upgrades beyond the currently planned program, such as beam polarization and ultra-high luminosity and so possibly  $L_{peak}$  in excess of  $1 \times 10^{36} \text{ cm}^{-2} \text{s}^{-1}$ . While the beam polarization has a concrete proposal, for ultra-high luminosity studies have just started.

At time of writing we are in the period of a long shut-down (LS1), last since June 2022 and the installation of a complete pixel detector (PXD) is almost done. The restart of data taking is planned at the beginning of 2024.

## 2. Belle II Upgrade

This second chapter wants to address some of the main reasons in favor of the upgrade of Belle II. We will give an overview of the primary background sources in the experiment to understand how to mitigate them in order to achieve a better performance of the whole detector, even ramping up the luminosity. Eventually we will also introduce some of the proposals made for the enhancement of the vertex detector.

[INTRODUCTION FROM CDR - OVERVIEW]

### 2.1 Background sources and limitations in Belle II

SuperKEKB is already the world's highest-luminosity collider and it aims to reach a new peak in the near future and also to increase the collected statistics, to become more sensitive to rare processes and precise measurements of Belle II physics program. But to be able to do this without losing the good functionality of the entire detector, it is necessary to understand how to reduce the beam background where possible and how to cope with the consequent challenges.

Several simulations and measurements of beam background are still being done in order to guess possible future machine scenarios, under new luminosity conditions. This is necessary to study the vulnerability of the subdetectors (and more generally of the machine) and so to design the countermeasures to adopt against the deterioration of performance and materials.

#### 2.1.1 Major background sources

In the following some of the primary *beam-induced* and *luminosity-dependent* background sources are listed.

**Touschek effect** : It is an intra-bunches scattering process, where the Coulomb scattering of two particles in the same beam bunch causes a variation of their energies, increasing the value of one of them and lowering that of the other from the nominal value. This interaction among the bunch particles is the first beam background source at SuperKEKB.

**Beam-gas scattering** : this represents the collision of beam particles with residual gas molecules in the beam pipe. It is the second beam background source and it can occur via two processes: *Coulomb interaction*, which changes the direction of the beam particles and *bremsstrahlung scattering*, which instead decreases their energy.

Because of these two processes, the scattered particles fall out the stable orbit and hit the beam pipe while they move around the ring. This mechanism causes electromagnetic showers that could reach the detector if their origin (loss position) is close to it.

**Radiative Bhabha scattering and two-photon processes :** There are several undesirable collision processes at the IP which have very high cross sections but only little interest for the physics studied in the experiment. Two of them are **Bhabha scattering** ( $e^+e^- \rightarrow e^+e^-\lambda$ ) and **two-photon processes** ( $e^+e^- \rightarrow e^+e^-e^+e^-$ ). In the first channel the emitted photon interacts with the iron magnets and produces a very large amounts of neutrons via the photo-nuclear resonance mechanism (such neutrons are the main background source for the outermost Belle II detector). The electrons-positrons pairs of the latter instead, can spiral around the solenoid field lines and leave multiple hits in the inner layers of the detector.

These processes increase the Belle II occupancy and radiation dose and they are referred as *Luminosity background* because their strength is proportional to the luminosity. The future upgrade intends to deal with this problem in order to keep occupancy low, even with higher radiation levels.

**Synchrotron Radiation (SR) :** X-rays emitted from the beam when electrons and positrons pass through the strong magnetic field near the IP. The HER beam is the main source of this type of background, because SR power is proportional to the square of beam energy and magnetic field. SR can potentially damage the inner layers of the vertex detector due to an higher radiation dose in that region. As a matter of fact, many current studies aim to enhance radiation hardness of the detector.

Making clear that even the intentional interaction of the beams is a source of noise for the measurements, there are also other background sources beyond those mentioned above and during the last decade a well-structured set of countermeasures have been developed trying to ease each one of them.

### 2.1.2 Current background status and future predictions

Several monitoring devices are located all along the accelerator to keep under control radiation doses on both detector and delicate regions of the ring, in such a way to intervene as soon as possible in case too high levels are reached. Indeed large doses of radiation could cause accidental damages on the detector, decreasing its performance.

A lot of dedicated beam background studies have been performed and for example, in Figure 2.1 are shown rates measured in June 2021 with a betatron function at the IP of  $\beta_y^* = 1$  mm and a collision luminosity of  $L = 2.6 \times 10^{34} \text{ cm}^{-2}\text{s}^{-1}$ . Current background rates in Belle II are acceptable and in most cases, well below the limits listed in table 2.2.

Event though the current level is of no concern in terms of occupancy for the innermost layers of the vertex detector, in the case of a larger amount of SR,

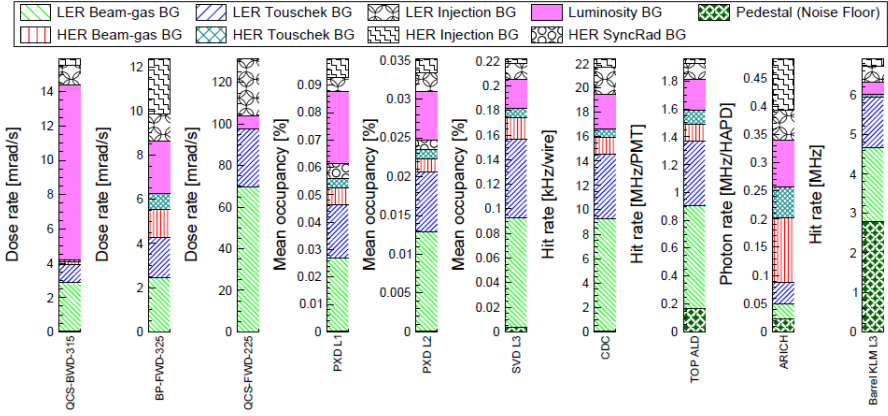


Figure 2.1: Measured Belle II background in June 2021. Each column shows different background sources for Belle II sub-detectors and also for superconducting quadrupole magnet (backward and forward) and the beam pipe.

Detector	BG rate limit	Measured BG	
Diamonds	1–2 rad/s	< 132 mrad/s	
PXD	3 %	0.1 %	
SVD L3, L4, L5, L6	4.7 %, 2.4 %, 1.8 %, 1.2 %	< 0.22 %	
CDC	200 kHz/wire	22.3 kHz/wire	
ARICH	10 MHz/HAPD	0.5 MHz/HAPD	
Barrel KLM L3	50 MHz	4 MHz	
non-luminosity BG			
Before LS1		After LS1	
TOP ALD	3 MHz/PMT + luminosity BG	5 MHz/PMT	1.8 MHz/PMT

Figure 2.2: Background rate limits for Belle II detector sub-systems. The third column shows the total measured background rate in June 2021.

for example, it may cause inhomogeneities in PXD module, which would make more difficult to compensate them by adjusting the operation voltages of the affected ones.

Until now it can be said that SuperKEKB and Belle II are operating stably. Beam-induced background rates are well below the limits of the detector and do not prevent from increasing further the current and hence the luminosity, as demonstrated by the predictions for the background rates *before LS2* with a known machine configuration. For what concern the predictions at  $L_{ist} = 3 \times 10^{35} \text{ cm}^{-2} \text{s}^{-1}$  instead, called *after LS2* operation, there are several uncertainties tied to the machine configuration. In fact at the moment, the *working machine lattice* to reach the target luminosity is not known and in addition the final design of the IR and beam pipes is not concluded yet.

Therefore an alternative solution is employed to roughly estimate the back-

ground rates. The background predicted Before LS2 phase is considered as a starting point and then different scaling factors are applied for single-beam background component, considering three different possible scenarios:

- **x2 - optimistic Scenario-1(v1)**
- **x5 - nominal Scenario-2(v2)**
- **x10 - conservative Scenario-3(v3)**, an arbitrary factor assuming that all single-beam backgrounds will be increased by a order of magnitude After LS2.

These are then used to simulate the behaviour of the whole detector in future perspectives, as we will see in the following.

## 2.2 Purposes of the upgrade

Current studies foresee that SuperKEKB may reach higher luminosity targets with the existing accelerator complex, but in order to achieve the established final value of  $6 \times 10^{35} \text{ cm}^{-2}\text{s}^{-1}$ , an enhancement of the interaction region are under consideration.

Belle II detector is also designed to operate efficiently under the high levels of backgrounds extrapolated to luminosity target, but safety margins are not so large. Moreover in the case of a redesign of the interaction region large uncertainties in the background extrapolations are unavoidable.

Therefore the global upgrade program is justified by many considerations, among them:

- improve detector's resistance to higher levels of background;
- make each subdetectors long-lived against radiation damage;
- push forward safety margins for running at higher luminosity;
- develop the technology to cope with different future paths;
- improve overall physics performance.

In particular all different upgrade ideas of the whole Belle II detector intend to ensure its proper functioning at the higher level of luminosity, condering also further improvements of the lattice machine and so of the colliding beams. Indeed current detector configuration is not expected to maintain its performance level when facing higher beam background level or higher rates.

In regards to the Vertex Detector, all proposed improvements aim to:

- reduce occupancy level by employing fully pixelated and fast detector (nowadays CMOS technology has been chosen);
- increase robustness against tracking efficiency and resolution losses from beam background;

- improve radiation hardness for delaying detector ageing effects and so performance degradation;
- reduce the inserted material budget between subdetectors in order to achieve good resolution by lessening the multiple scattering, above all at lower momenta.

## 2.3 Summary of possible VXD upgrade

The Vertex Detector is particularly sensitive to machine background because it is the closest to the beam pipe and therefore subject to high doses of radiation. As we have already seen, current studies are trying to extrapolate how it could be affected by reaching the future luminosity target, but there are a lot of uncertainties due to models and still not well defined design of the interaction region. Moreover a completely new detector might be required, in event of a considerable redesign of the IR. However in this case, also the physics performance could be improved, taking advantage of the more recent technology developments.

In the following we will present in a few words the four main proposal for future upgrade: Depleted Field Effect Transistor (DEPFET) pixel, thin sensor, CMOS Monolithic Active Pixel Sensor and SOI technology. The first two are more conservative and try to exploit as much as possible of the existing detector, making some appropriate adjustments to the sensor type, readout or mechanical structure. The last ones instead, plan to build an entirely new detector.

During the design of all of them, some reference radiation levels have been considered to ensure that the background robustness of the innermost layers is suitable:

- Hit rate capability:  $120 \text{ MHz}/\text{cm}^2$ ;
- Total Ionizing Dose:  $10 \text{ Mrad/year}$ ;
- NIEL fluence:  $5 \times 10^{13} n_{eq}/\text{cm}^2/\text{year}$ .

### 2.3.1 Depleted Field Effect Transistor (DEPFET)

This first proposal intend to minimize risks and costs of the project, preserving the general layout of the PXD system. The upgrade consists to improve the sensor above all, in order to provide higher safety factor for the allowed occupancy and to prevent some issues that at the moment weaken the good functionality of the detector.

Some of the main improvements are listed below:

- improve signal transmission on the pixel matrix and the signal processing in the read-out, in order to reduce the read-out time per row from the current 100 ns to 50 ns. In this way the frame time and the background occupancy might be reduced by factor 2, while leaving unchanged the optimized size and number of PXD pixels as it stands;

- increase the robustness against beam losses which could make inefficient or even inoperative gate lines on almost all PXD modules. This reaction seems to be due to a high photocurrent on the chip because of the high instantaneous dose. It could be mitigated by adding protection circuits on-chip;
- Total Ionizing Dose (TID) effect on the chip provokes an unexpected avalanche current that does not compromise the sensor performance but requires more power supply to provide enough current. This issue might be solved by bringing some changes in the DEPFET pixel layout.

### 2.3.2 Thin and Fine-Pitch SVD

The Thin and Fine-Pitch SVD (**TFP-SVD**) is a new detector concept that aims to improve not only SVD, but also the inner part of the CDC, whose functionality could be threatened by future beam background condition. This proposal takes into account the Double-sided Silicon Strip Detector (DSSD) as a prime candidate for a tracking device in the inner and middle detector volume since a single sensor can cover a large dimension of about  $100 \times 100 \text{ mm}^2$ . In the current detector the DSSD technology is already used in the SVD, which deals with vertex reconstruction and low momentum tracking, together with PXD.

One of the major improvements of this technology is the reduction of the material budget. Currently SVD has about  $0.7\%X_0$  material budget per layer. TFP-SVD instead, decreasing the sensor thickness to  $140 \mu\text{m}$ , intend to reduce it to  $0.41\%X_0$ .

Moreover small sensor thickness is expected to reduce the voltage needed to reach the full depletion, even after radiation damage. The front-end thought for TFP-SVD (SNAP128) has 128 input channels and a 127 MHz clock in each of them, to generate the binary hit information sampled. It also offers a reduction of the amount cables.

Some concerns about TFP-SVD are the feasibility and efficiency of the final sensor production and the small signal charge due to the short path length of the particles through the sensor.

In any case a first prototype has been produced by Micron-Semiconductor Ltd (UK), with a size of  $52.6 \times 59.0 \text{ mm}^2$ . The characterization studies are in agreement with the expectation and also a lower full depletion voltage is confirmed. It is planned to increase the dimensions to  $100 \times 100 \text{ mm}^2$  in the further prototype.

### 2.3.3 Silicon On Insulator (SOI)

The basic idea of the proposal is to replace the whole VXD detector employing a new design of pixel, called Dual Timer Pixel (DuTiP), based on SOI technology. This new sensor concept has been invented to cope with the expected higher background accordingly to higher value of luminosity ever achieved.

#### Concept

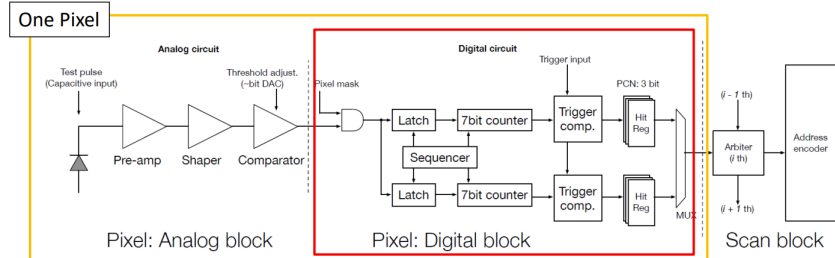
SOI technology has been chosen as baseline for the new pixel design thanks to its monolithic structure, thinness, low power consumption and low parasitic

capacitance. In addition it is resistant against neutron and single event upset (SEU<sup>1</sup>), even though an important issue is TID effect on which efficient solutions have been studied.

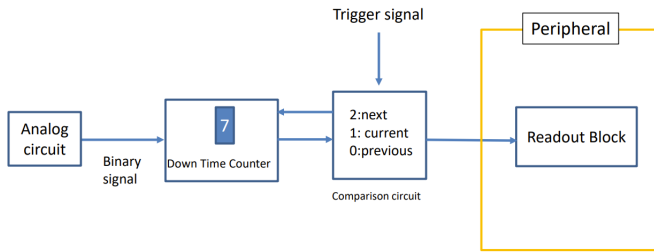
DuTiP has been invented to fulfil the requirements of a new vertex detector with faster readout, lower occupancy, smaller data size and smaller data transfer. In particular its concept rest on the concern to store at least two hits during Belle II trigger latency ( $5 \mu\text{s}$ ), to avoid loss information of the inner part of the detector in higher background environment.

The analog part is quite standard for a binary detector and consists of a sequence of preamplifier, shaper and comparator. Digital part is equipped with two timers (7 bit counters) to store at least two hits. When a processed hit signal arrive to the digital part it is stored and one of the timers start to counting down from a starting time set to trigger latency plus one clock, waiting for trigger signal. If the trigger signal is received when the time is 1 (it could be also 2 or 0), the signal is readout as *Current* (*Next* or *Previous* respectively) timing (*PCN timings*). If the trigger is not received at the PCN timings in the pixel, the timer is reset.

This complicated digital circuit has to be assembled on each pixel and Lapis semiconductor  $2.0 \mu\text{m}$  FD-SOI CMOS technology has been chosen, based on the experience gained in the successful development of other detectors like pixel detectors for the future ILC (SOFIST) and CEPC.



(a) Analog, Digital and Scan blocks for DuTiP detector.



(b) Operational sketch.

Figure 2.3: Schematic of DuTiP circuits.

---

<sup>1</sup>A Single Event Upset (SEU or SEE, Single Event Error) occurs when a ionizing particle deposits charge close to a storage node (e.g. RAM cell, register) causing a bit value to flip leading to corrupt information. This effect could be mitigated by using, for example, redundant memory. It is not a permanent damage.

### Sensor design and features

The size of the new designed pixel is  $45 \mu\text{m}$  and the sensor layer thickness of  $50 \mu\text{m}$ , which gives an intrinsic resolution better than  $15 \mu\text{m}$  on  $z$  direction averaging over incident polar angle. ALPIDE was chosen as analog circuit with some modification to adapt it to SOI technology.

DuTiP pixel detector is designed to cover the current VXD acceptance with 7 layers: 1-3 with S (smaller size chip) type sensors, 4-7 with L(larger size) type (Figure 2.4).

sensor type	layer	pitch [ $\mu\text{m}$ ]	row $\times$ column [pixels]	array $r\phi \times z$ [ $\text{mm}^2$ ]	array area [ $\text{cm}^2$ ]	chip $r\phi \times z$ [ $\text{mm}^2$ ]
S	1-3	45	$320 \times 640$	$14.4 \times 28.8$	4.15	$17.2 \times 29.6$
L	4-7	45	$480 \times 640$	$21.6 \times 28.8$	6.22	$24.4 \times 29.6$

Figure 2.4: The size of Small (S) and Large (L) DuTiP chips.

Stitching technique allows to produce longer chips in the  $z$  direction, but the structure of the ladders has not been decided yet. Anyway the target is to minimize the dead region between chips in the ladder. For the inner layer of the detector might be possible the cooling with airflow at room temperature; for the outer layers instead, a combination of air and water flows.

For layer 1, which is expected to work in more severe condition of background, the pixel occupancy has been estimated with the trigger latency of  $8.0 \mu\text{s}$  and for both L and S type it is small enough,  $O(10^{14})$  or less, thus stable tracking and vertexing are contemplated. Moreover without using two timers for layer 1, the signal loss probability with the trigger latency of  $4.5$  ( $8.0$ )  $\mu\text{s}$  is about  $0.2$  ( $0.4$ )% and so not negligible. In fact if the background rate is higher and the latency is longer, the signal loss probability increases.

The first prototype of this new chip has been delivered in June 2021, with all in-pixel functionalities except for the scan block and the fast readout system. The chip is a matrix of  $64 \times 64$  pixels and size of  $6 \times 6 \text{ mm}^2$ . Its characterization is ongoing and it seems to work fine, also with radioactive sources and red laser tests.

The second prototype DuTiP2 had been delivered in 2022, with  $32 \times 320$  pixels and size of  $17.2 \times 6 \text{ mm}^2$ . It has all functionalities except for fast hit data collection to periphery. The phase of testing is ongoing. A third prototype has been submitted in 2023 and will be delivered in 2024 (all prototypes shown in Figure 2.5).

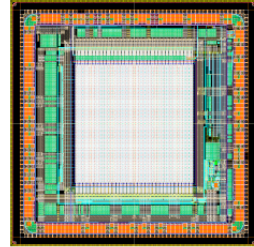
#### 2.3.4 CMOS Monolithic Active Pixels Sensor

The last proposal is the one that we will analyze in more details in the next chapter. Like the previous one, it aims to replace the entire current VXD detector using a new technology, in this case the Monolithic Active Pixel Sensor CMOS (Complementary Metal-Oxide Semiconductor).

The program hopes to solve some of the issues discussed in the previous chapters, with a new system of two inner layers and three outermost, for a total of 5 stages equipped with a single sensor type, called VTX (layout in Figure 2.6). Also the



(a) DuTip1 prototype on the left and DuTip2 on the right.



(b) DuTip3 third prototype.

Figure 2.5: DuTip prototypes.

mechanical structure has been redesigned but it is expected that the all system could work at room temperature, so as consequence an important reduction of services is also contemplated.

The new pixel design is called OBELIX (Optimized BELle II pIXel sensor), based on the pixel matrix of the TJ-Monopix 2 chip, whose characterization is the main topic of this work (Chapter 5).

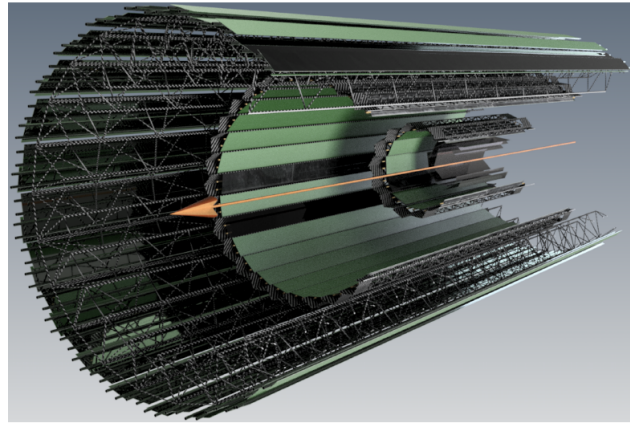


Figure 2.6: Overall VTX layout.

The VTX solution intends to reduce the current PXD integration time by at least two order of magnitude and also other advantages are expected:

- lower detector occupancy which allows to cope with higher background

and to mitigate any data-transmission bottleneck.

- Better tracking efficiency and improved momentum resolution and impact parameter resolution at low transverse momentum.
- Smaller data cables cross sections and less complex cooling system which might lighten the needed services.
- Control and power systems become unique due to the employment of a single sensor chip for all layers.

At the current state of art intense R&D (Research and Development) is being carried out, taking advantage from other experiments experiences like ALICE, with the same type of sensor.

Among all these options that we sift through, the last one has been chosen for the future upgrade of the vertex detector. The first two proposals have now been abandoned, the one that contemplates the use of the SOI technology instead, is considered as a backup option.

After this briefly review of the main upgrade proposals, we can now deepen into the VTX program in the following chapter.

## 3. VTX detector

This chapter focuses on one of the four proposals for the vertex detector upgrade of Belle II, that is VTX. After a brief reference to the reasons behind the vertex detector upgrade, we will go through VTX concept and layout, designed with a new geometry with respect VXD and also with a different mechanical structure and new pixel sensors (OBELIX), needed to fulfill the new requirements dictated by new environment conditions. Moreover all ongoing studies are supported by continual tests and simulations that we will also take a look at.

### 3.1 VTX Layout and mechanical structure

In subsection 1.2.2 we have introduced in a few words the concept of the *nano-beam* scheme, which could allow to achieve the new target of instantaneous luminosity. This new strategy requires a strong focusing of the beams in particular at the IP, resulting in a large amount of beam induced background and as consequence in a higher dose of radiation in the innermost detector layers. Therefore they have to be robust enough to keep good performance against these new hard conditions. Furthermore to be able to increase the luminosity, SuperKEKB might have to consider an improvement of the final focusing magnets and so a potentially re-design of the interaction region, including the detector but independently of its hit rates and radiation hardness issues.

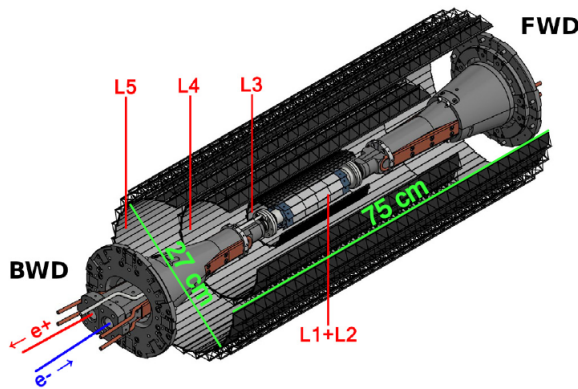


Figure 3.1: Concept of VTX layout with 5 barrel layers, filling the current VXD volume.

VTX project aims to replace the all VXD with a fully pixelated detector based on Depleted Monolithic Active Pixel Sensors (DMAPS) arranged on five layers at different distance from the beam pipe. Actually the radii and the number of the layers are currently subject to several studies and simulations, in order to achieve an optimized arrangement (Figure 3.1). For now two layers are planned in the innermost part (*i*VTX) and three in the outermost (*o*VTX). The active lenght of the ladders is expected to vary from 12 to 70 cm to cover the required acceptance of  $17^\circ < \theta < 150^\circ$ .

As already discussed for the other upgrade proposals, it is important to try to reduce the material budget, in order to minimize the multiple Coulomb scattering which particularly affects the very soft particles produced in Belle II collisions. By using a single sensor type, it is expected a reduction of the overall material budget up to 2% of radiation lenght, against the present 3% of VXD, which uses two different sensors such as pixels and strips.

### 3.1.1 iVTX

The *internalVTX* consists of the first two detector layers devised together with a self-supported air-cooled all-silicon ladder concept, where four contiguous sensors are diced out of a wafer, thinned and interconnected with post-processed redistribution layers. They are designed to be at 1.4 and 2.2 cm respectively from the beam pipe, and target an individual material budget of about 0.1% radiation lenght. This is actually achievable because the overall surface of these layers is moderate, below  $400\text{ cm}^2$ , as well as the sensor power dissipation is expected to be low and the connections needed for the operation to be a few. Precisely for these reasons, air cooling could be a workable system to avoid overheating.

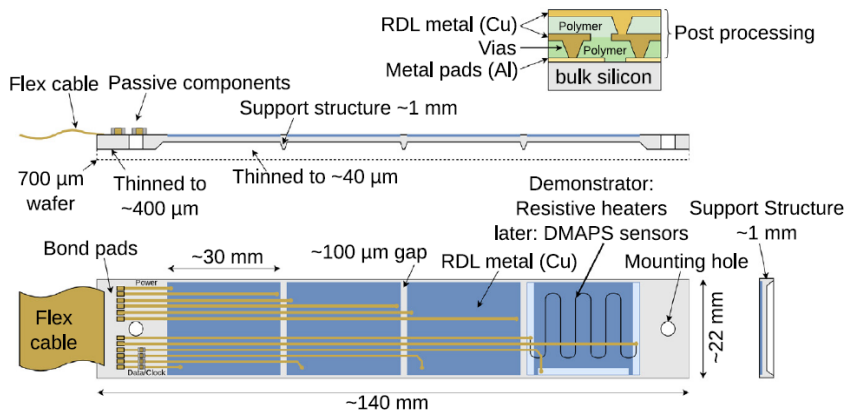


Figure 3.2: Sketch of the all-silicon ladder concept of the iVTX. Four dummy sensors are shown in blue on the silicon support in grey. The yellowish lines instead, indicate power and data transmission lines. Power is delivered to the ladder by a flex cable, which also transmits data to and from the chips in the final one.

The ladder has to be equipped with four of the aforementioned OBELIX chips and thinned to  $50\text{ }\mu\text{m}$  except in some border regions, where a few hundreds

of  $\mu\text{m}$  are necessary to ensure mechanical stability. In order to interconnect the sensors along the ladder and provide a unique connector at the backward end, during the post-processing metal strips are etched on the redistribution layer (RDL). The latter has the main purpose to route power and data via impedance-controlled transmission lines to a flex cable, added at the end of the ladder. After the RDL processing, the backside of the ladder has to be thinned in accordance with what was previously mentioned. Mounting holes will be added via laser-cutting.

In Figure 3.2 is displayed a sketch of the iVTX demonstrator ladder (currently under production), 140 mm long and 22 mm wide (grey). Instead of the actual sensors, it is equipped with four dummy chips with a length of about 30 mm (blue), which are used as resistors to mimic the estimated heat load in order to test the air cooling system and more generally to characterize the electrical, mechanical and thermal performance of the ladder. A redistribution layer for power and data is also added to the demonstrator, in order to connect the chips with a flex cable at the end of the ladder (yellowish lines). In addition the wafer is thinned to 400  $\mu\text{m}$  and the sensitive areas down to 40  $\mu\text{m}$  with the purpose to test the mechanical integrity of the whole structure.

## R&D

The R&D is ongoing and the full-silicon ladder concept is currently being assessed with industrial partners. First thinned ladders have been produced and characterised with different thickness and geometry.

Furthermore several tests are focused on evaluating power delivery efficiency, the quality of the signals which travel through the ladder and also the process used to fully assemble it. In Figure 3.3 are shown eye diagrams from simulation with a transfer rate of 640 Mbps, which may imply that 320 Mbps of data rate will be possible.

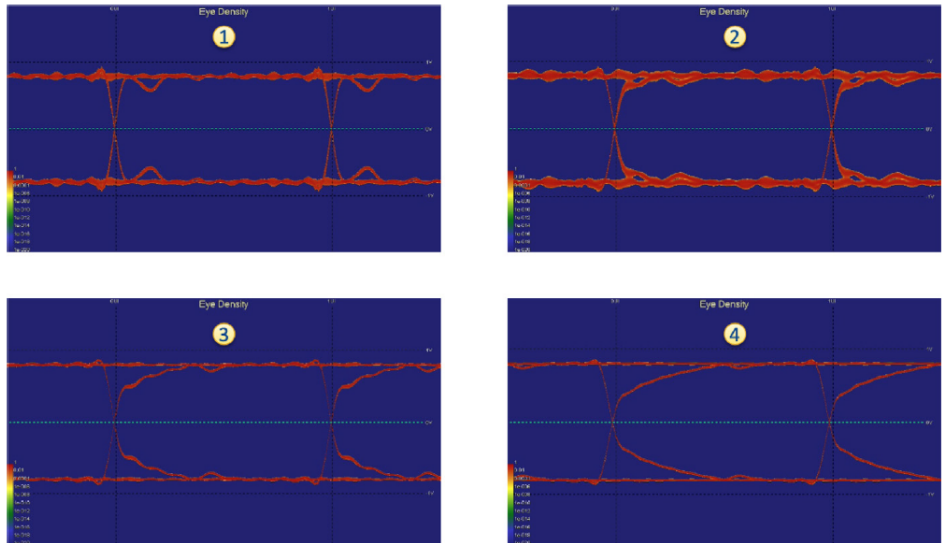


Figure 3.3: Eye diagrams of the iVTX data transmission lines at four different locations on the ladder.

Moreover it has been demonstrated that air at the temperature of 15° and flowing with a speed of 10 m/s succeeds to cool a single inner module, assuming power is uniformly dissipated on the sensor surface. The maximum temperature reached is 20°C.

Through very first estimates it is expected that an equivalent section of 6 tubes with 10 mm of diameter is necessary to expel the heat from the inner layers, roughly equal to 65 W. So it is essential to design a mechanical structure which provides for the space needed to the tubes in order to bring the air at the IP and also compatible with the new interaction region.

### 3.1.2 oVTX

The **outer VTX** consists of three layers respectively at radii of 39 or 69, 89 and 140 mm from the beam pipe and because of the larger distance required to cover the acceptance, they are not self-support. They follow a more traditional approach, strongly inspired by the design developed for the ALICE ITS2. Each ladder is water cooled and made of a light carbon fiber support structure, called ***truss***, which provides the mechanical integrity. Its structural design is shown in Figure 3.4 : 70 cm long and 5.8 g of weight, it is able to support more than 40 sensors in two rows next to each other with a small overlap, earning a material budget of 0.3%  $X_0$  for the first two layers and 0.8% $X_0$  for the outermost one.



Figure 3.4: Prototype of the layer 5, called *truss*, which is the longest, made from thin carbon fibre structures.

For the cooling of the ladder a cold-plate concept is under development (Figure 3.5), on which the sensors are glued and that in turn is installed on the *truss*. For each row there is a polyimide cooling tube that runs over all the sensors and turns back at the other end, so that the heated coolant leaves on the same side. Then two flex print cables connect the two halves of the ladder to the connector.



Figure 3.5: A prototype of the cold-plate for cooling. One coolant tube(golden) is connected to the cold plate(black) and turns 180° on the other end (not shown) so that the coolant flows in both directions and thus leaves on the same side it starts.

For layer 3 instead, only one flex print cable in the backward side is considered, in order to leave more space in the forward for other possible services and accelerator components. As mentioned above, for the third layer two different solutions are under study: at radius of 39 mm e 69 mm respectively. In Figure 3.6 are displayed schematic examples of some hypotheses.

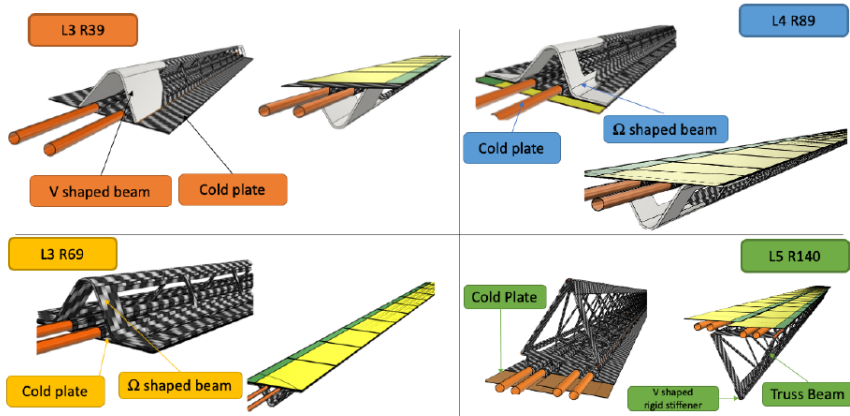


Figure 3.6: Schematic view of possible solutions for the three outermost layers.

In Figure 3.7 are shown the several substructures described before, that shape a ladder of the outermost layer 5. From bottom to top come in succession the carbon fibre structure, two cold-plates for the two neighbouring sensor rows (indicated as "Chips", in grey) and the flex cables for power and data transmission (green).

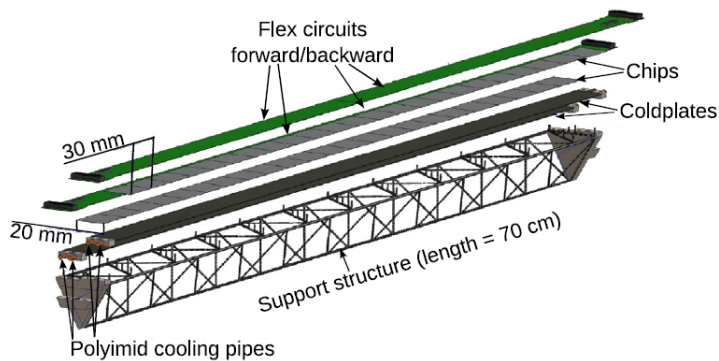


Figure 3.7: An exploding drawing of a fully assembled layer 5 ladder.

## R&D

The carbon fiber support structure and flex cable have been designed and fabricated for the last ladder, which is also the longest. Also services for the last two ladders, like electrical connections and cooling, can be provided both

on forward and backward sides. A Multiline Power Bus has been realized in order to power each OBELIX chip along the ladder by a dedicated VDD and GND pair.

After the assembly described in the previous, first thermo-mechanical tests have been performed and they show that the first resonance frequency is at 200 Hz, which is safely far from the one of the typical earthquakes in Japan, and also that the thermal properties are good.

Trying to reduce as much as possible the material budget, the transmission lines and the flex cables have to be as thin as possible, but they also have to ensure safe data transmission. Trace widths are trimmed to fulfill the same maximum voltage drop requirement (200 mV) for all the chips.

For this reason, the outermost ladders (70 cm long) are equipped with two flex cables, one from each side of the *truss*. In Figure 3.8 the resulting eye diagram from testing the signal integrity of one of the 35 cm long transmission lines for data transmission rate of 500 Mbps. This result demonstrates that the bandwidth is large enough to allow more than needed 160 Mbps for data transmission.

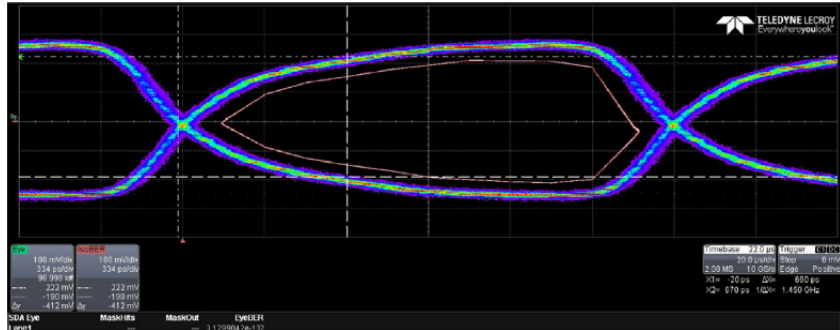


Figure 3.8: Eye diagram for the oVTX transmission line signal integrity of the layer 5 flex cable.

In addition, thermal tests have been performed for the last layer prototypes using kapton heaters to emulate the power dissipation of the chips. The coolant (demineralized water) has been set to a temperature of 10° at the beginning, the environment at 20° with a negative pressure of 0.2 bar. Results have been demonstrated that for three different configurations of the flow (such as monodirectional, bi-directional and with an U-turn at one end) the average temperature stands at 24° with a maximum gradient of  $\Delta T \approx 4^\circ$  along the full lenght of the ladder.

All these investigations validate the design of the longest ladder, which is indeed the most challenging, and therefore the possibility to operate the chips safely.

### 3.1.3 Thermomechanics and data transmission

The proposed VTX detector intends to employ the same sensor type for all the layers in order to use a unique control and power supply system. It is expected

to operate at room temperature and for what we have seen in the previous, the smaller cross section of data cables, the usage of optical fibers and the less complex cooling system might allow a considerable reduction of services with respect to the current VXD. This allows more room for maneuver in the design of the new IR, needed for ramping up the instantaneous luminosity in the future.

As consequence also the design of the mechanical support system, data cables and acquisition system required could be more simple and in particular, the standard PCIe40 acquisition boards used in Belle II match well the data throughput requirement.

## 3.2 Performance simulation

As we have seen in chapter 2, to reach a new peak of luminosity the experiment has to face also the consequences, like the higher level of machine related background and so larger doses of radiation, especially in the inner layers of the whole detector. For these reasons a lot of simulations and studies are focusing on ensuring that the main physics goals of the experiment will be achieved despite the more severe conditions to which it would be subjected.

The VTX upgrade program which foresees for a new silicon vertex detector with high granularity in both space and time, could bring significant improvements in tracking efficiency especially at low momentum, in the impact parameter resolution and in the robustness against backgrounds.

### 3.2.1 Potential VTX geometries

As we have already mentioned in the description of the possible VTX layout (subsection 3.1.2), two different VTX geometries are currently under study, which differ only in the position of the third layer (Figure 3.6).

The ***nominal*** geometry is expected to maximize the track impact parameter resolution and it places the third layer at 3.9 cm from the IP. The ***alternative*** geometry instead, aims to improve the  $K_S^0$  reconstruction efficiency and the third layer is located at 6.9 cm from the IP.

Several simulations and investigations are ongoing and they are comparing performance of these two different layouts with that of the current Belle II detector (utilizing a full Geant4 simulation of the detector in the study of specific decay modes of interest). Moreover, the different machine background predictions are also examined in order to consider all effects and correlations.

### 3.2.2 Tracking efficiency at low momentum and impact parameter resolution

Tracking efficiency at low momentum is one of the areas where the VTX upgrade scenarios show more promising results, particularly for the *soft pions* originated from the decays of  $D^{*\pm}$  mesons.

Studies are based on the reconstruction of the decay chain  $B^0 \rightarrow D^{*-} l^+ \nu$ , with  $D^{*-} \rightarrow \bar{D}^0 \pi_{soft}^-$  and  $\bar{D}^0 \rightarrow K^+ \pi^-$  or  $K^+ \pi^- \pi^+ \pi^-$ . All background scenarios mentioned in subsection 2.1.2 are considered in the evaluation of the ***nominal*** VTX performance and they are compared with the nominal Belle II geometry

in the intermediate (**v2**) background hypothesis. In table 3.9 is shown what has been obtained.

	Belle II (v2)	VTX (v1)	VTX (v2)	VTX (v3)
Generated events	32533	32559	32559	30255
Correctly reconstructed signal	10059	16913	16848	15583
Combinatorial	28495	51375	51826	47527
Efficiency	30.9%	51.9%	51.7%	51.5%
Purity	26.1%	24.8%	24.5%	24.7%

Figure 3.9: Reconstruction efficiency and purity for the the decay chain  $B^0 \rightarrow D^{*-} l^+ \nu$ , with  $D^{*-} \rightarrow \bar{D}^0 \pi_{soft}^-$  and  $\bar{D}^0 \rightarrow K^+ \pi^-$ , for the nominal Belle II detector at the intermediate background conditions (**v2**) and the nominal configuration of VTX in all three background scenarios.

We can see that the VTX reconstruction efficiency<sup>1</sup> in all three background hypotheses, results to be improved of almost a factor 1.7 with respect to the nominal Belle II, with comparable purity<sup>2</sup>. Moreover efficiency remains practically stable in all background conditions, even in the most severe one.

This enhancement in tracking efficiency relies in particular on improved tracking efficiency for the  $\pi_{soft}^-$  mesons, as we can see in Figure 3.10.

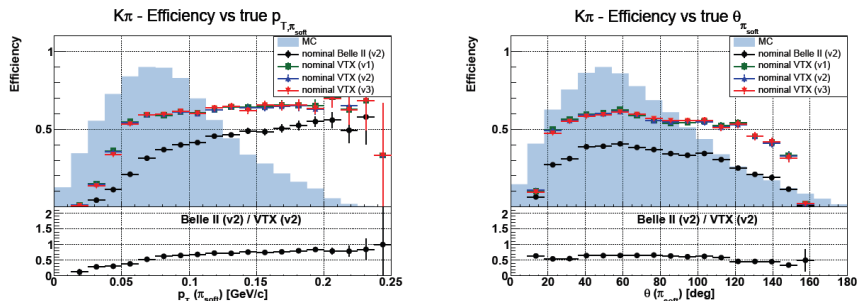


Figure 3.10: Reconstruction efficiency of  $B^0 \rightarrow D^{*-} l^+ \nu$  as a function of the transverse momentum of the  $\pi_{soft}^-$  (from  $D^{*-} \rightarrow \bar{D}^0 \pi_{soft}^-$ ) in the plot on the left and of the polar angle of the  $\pi_{soft}^-$  on the right. The shaded blue histograms represents the momentum spectrum of the  $\pi_{soft}^-$ . The nominal Belle II geometry efficiency in the intermediate background scenario (**v2**) is represents by black dots and it is compared with the nominal VTX configuration in the optimistic (**v1**, green squares), medium (**v2**, blue upward pointing triangles) and pessimistic (**v3**, red downward pointing triangles) background hypotheses. The bottom plots show the ration between nominal Belle II and nominal VTX in the **v2** background scenario.

For all scenarios with nominal VTX, there is a powerful improvement for transverse momenta below 0.05 GeV/c, with respect to the nominal Belle II.

<sup>1</sup>Efficiency is defined as the ration between the number of correctly reconstructed signal events and the total number of candidates.

<sup>2</sup>In a few words, the probability that a correctly reconstructed signal is a "signal event".

Only for  $p_T$  greater than 0.2 GeV/c the reconstruction efficiency of Belle II approach those of the VTX.

For  $p_T$  higher than 0.3 GeV/c instead, the momentum resolution is dominated by the CDC and there is not a significant enhancement in track momentum resolution considering the preceding example.

### 3.2.3 Vertexing resolution

Studies on vertexing performance have been conducted using samples of one million  $B^0 \rightarrow J/\psi K_S^0$  events generated and reconstructed with all the aforementioned combinations. The distributions of the decay vertex resolution  $\sigma_z$  (i.e. the width of the distribution obtained considering the differences between the measured and the true simulated positions) along the  $z$  axis of the B decay signal are shown in Figure 3.11.

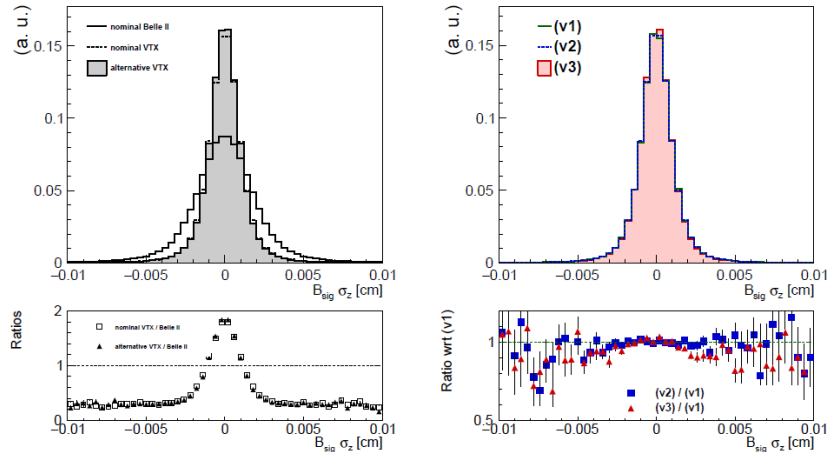


Figure 3.11: On the left: comparison of the B decay vertex resolution along the  $z$  axis in  $B^0 \rightarrow J/\psi K_S^0$  events for the nominal Belle II (solid line), nominal VTX (dotted line) and alternative VTX geometry (filled grey histogram). The bottom plot shows the ratio between the VTX geometries (empty squares the nominal one and filled triangles the alternative) and nominal Belle II.

On the right: B decay vertex resolution along the  $z$  axis for the nominal VTX geometry in the three background scenarios: optimistic **v1** (green solid line), intermediate **v2** (blue dotted line) and pessimistic **v3** (red filled histogram). The bottom plot represents the ratio between the two higher background scenarios and the optimistic one.

In table 3.12 a summary of the results that shows that the new geometries achieve a better resolution on the B decay vertex of about 35% on average and they also do not suffer of any significant degradation as the background conditions varies, unlike the nominal Belle II configuration.

The VTX geometries have been demonstrated to achieve better performance also for the vertexing resolution along the  $x$  and  $y$  axes. Also in these directions they turn out to be almost insensitive to the different levels of background.

$B_{sig}$ z vertex resolution ( $\mu\text{m}$ )	Bkg (v1)	Bkg (v2)	Bkg (v3)
Belle II	21.9	23.0	24.9
Nominal VTX	14.5	14.4	14.1
Alternative VTX	14.4	14.3	14.0

Figure 3.12:  $B_{sig}$  vertex resolution along the  $z$  axis for the three detector layouts and the three background scenarios.

Similar studies for the  $K_S^0$  decay vertex resolution are displayed in Figure 3.13 and in the same way, the upgraded geometries reach a better vertexing resolution with respect to the nominal Belle II detector without any significant degradation as the backgrounds increase. It is important to notice that in the right plot there is a spurious effect that cause an apparent improvement of performance in the worst case scenario among those considered. This is due to the loss of reconstruction efficiency for candidates with large flight distance (thus affected by poorer vertex resolution).

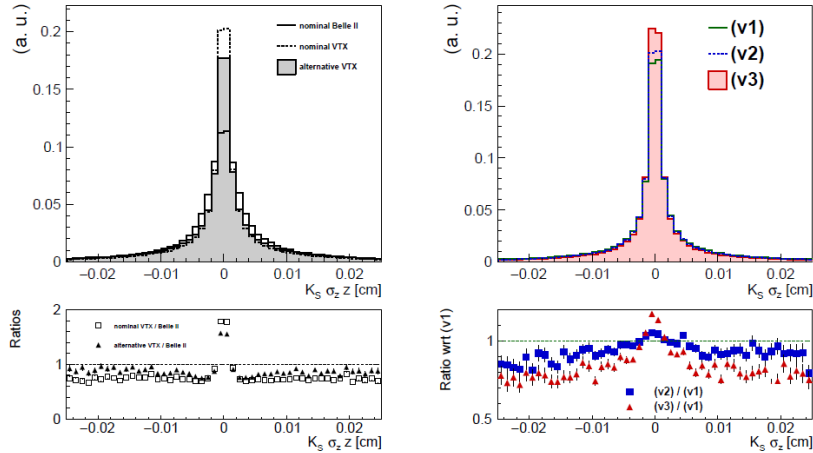


Figure 3.13: On the left: comparison of the  $K_S^0$  decay vertex resolution along the  $z$  axis in  $B^0 \rightarrow J/\psi K_S^0$  events for the nominal Belle II (solid line), nominal VTX (dotted line) and alternative VTX (filled grey histogram). The bottom plot shows the ratio between the VTX geometries (empty squares for the nominal and filled triangles for the alternative) and nominal Belle II detector. On the right:  $K_S^0$  decay vertex resolution along the  $z$  axis for the nominal VTX in the three background scenarios: optimistic **v1** (green solid line), intermediate **v2** (blue dotted line) and pessimistic **v3** (red filled histogram). The bottom plot represents the ratio between the two higher background scenarios and the optimistic one.

### 3.3 OBELIX chip design

The VTX detector is designed with a single type sensor taylored to the specific needs of Belle II, called OBELIX (Optimized BELle II pIXel sensor) and currently under development, based on fast and high granular Depleted Monolithic Active Pixel Sensor (DMAPS). This new sensor design comes from an evolution of TJ-Monopix 2, whose characterization is the main topic of this thesis, and which will be discussed in chapter 5. Both of them are fabricated in a modified TowerJazz Semiconductor 180  $\mu\text{m}$  CMOS process, that matches particularly well the Belle II requirements. In particular TJ-Monopix 2 is equipped with four different flavors (??), which stand out for different type of collection electrode coupling and some small differences in the circuit design. For now their characterization are ongoing and the final decision on which to use for OBELIX has not been made.

#### 3.3.1 Sensor specification

A schematic layout of the chip is shown in Figure 3.14 . The size of the sensor is expected to be  $3 \times 1.9 \text{ cm}^2$ , with an active area of  $3 \times 1.6 \text{ cm}^2$  and an additional part in the periphery of about  $3 \times 0.3 \text{ cm}^2$  dedicated to data pre-processing and triggering. The pixel pitches<sup>3</sup> are designed to be from 30  $\mu\text{m}$  to 40  $\mu\text{m}$  in both direction. As a matter of fact staying in this range is necessary in order to achieve a spatial resolution below 15  $\mu\text{m}$ , wihch is a requirement of the VTX upgrade program.

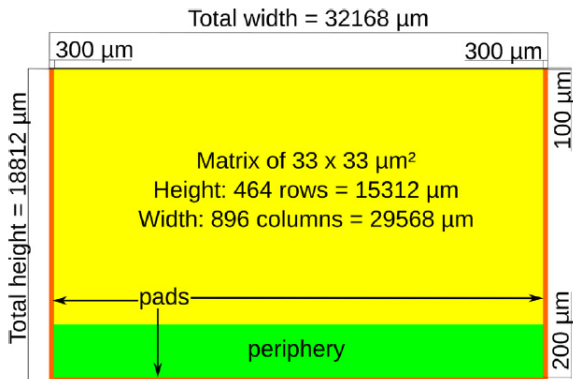


Figure 3.14: OBELIX chip design.

Moreover the sensor thickness has to be below 100  $\mu\text{m}$  to respect the material budget constraint of 0.2%  $X_0$  and as consequence the depleted sensitive region should be lower than 50  $\mu\text{m}$ , perfectly in agreement with the available thickness of MAPS technology. To deal with the target hit rate of 120 MHz/ $\text{cm}^2$ , the timestamp clock signal can reach down to 25 ns, even if studies have demonstrated that a window of 100 ns (*integration time*) is enough to limit to 320 Mbps the data throughput at the same expected hit rate. All topics faced above allow

---

<sup>3</sup>The distance between the centers of two contiguous pixels.

to realize a sensor with high granularity in both space and time.

With respect to TJ-Monopix 2, which is equipped with a triggerless column-drain readout without memory at the periphery, OBELIX must have a triggered readout architecture, in order to satisfy the needs of Belle II. Moreover the latency is fixed to 5(10)  $\mu\text{s}$  and it might operate up to 30 KHz trigger rate.

The expected power consumption instead, is expected to be about 200  $\text{mW cm}^{-2}$ , a value which should allow air-cooling for the small area corresponding to the two inner layers and liquid coolant for the outer ones.

Its main design features are summarised in Figure 3.15.

Pixel pitch	30 to 40 $\mu\text{m}$
Matrix size	512 rows $\times$ 928 to 752 columns
Time stamping	25 to 100 ns precision over 7 bits
Signal Time over threshold	7 bits
Output bandwidth	320 to 640 Mbps
Power dissipation	100 to 200 $\text{mW/cm}^2$
Radiation tolerance	100 MRad and $10^{14} \text{n}_{\text{eq}}/\text{cm}^2$

Figure 3.15: Designed features of the OBELIX sensor.

	Specification	TJ-Monopix2
Pixel pitch	< 40 $\mu\text{m}$	< 33 $\mu\text{m}$
Sensitive layer thickness	< 50 $\mu\text{m}$	30 $\mu\text{m}$ and 100 $\mu\text{m}$
Sensor thickness	< 100 $\mu\text{m}$	-
Hit rate capability in the matrix	> 600 $\text{MHz cm}^{-2}$	> 600 $\text{MHz cm}^{-2}$
Hit rate capability at the sensor output	> 120 $\text{MHz cm}^{-2}$	>> 100 $\text{MHz cm}^{-2}$
Trigger delay	> 10 $\mu\text{s}$	-
Trigger rate	30 kHz	-
Overall integration time	< 100 ns	-
(optional) Time precision	< 50 ns	-
Total ionizing dose tolerance	100 kGy/year	1 MGy/year
NIEL fluence tolerance	$5 \times 10^{13} \text{n}_{\text{eq}}/\text{cm}^2/\text{year}$	$1.5 \times 10^{15} \text{n}_{\text{eq}}/\text{cm}^2/\text{year}$
SEU tolerance	frequently ( $\text{min}^{-1}$ ) flash configuration	-
Matrix dimensions	around $30 \times 16 \text{ mm}^2$	$19 \times 19 \text{ mm}^2$
Overall sensor dimensions	around $19 \times 19 \text{ mm}^2$	$20 \times 19 \text{ mm}^2$
Powering	through voltage regulators	-
Outputs	one at < 200MHz	one at 160 MHz

Figure 3.16: Comparison between OBELIX requirements and TJ-Monopix 2 features.

### 3.3.2 Sensor implementation

The technical implementation of the OBELIX sensor have to match all main features listed in table 3.15 . As mentioned above, this new sensor is the development of Tj-Monopix 2, whose characteristics fit the Belle II requirements.

From Tj-Monopix 2 design, the pixel pitch of  $33 \times 33 \mu\text{m}^2$  is maintained, as well as the layout of both digital and analogue parts. Also the Time-Over-Threshold method to digitized the signal is preserved, with a bus width of 7 bit, together with the column-drain readout architecture implemented for pairs of columns. Other features which will be explained in depth in chapter 5, have been conserved in the new design like the 3-bit register dedicated to the threshold

tuning, but with a larger range of correction. Moreover to aim at the integration time of  $100 \mu\text{s}$ , the clock frequency which defines the precision of ToT and BCID (that is the timestamp), has been decreased from 40 to 20 MHz. So the current baseline for OBELIX timestamp precision is 50 ns.

However two new modules are added to the implementation, related to the Belle II trigger: the Trigger Logic Unit (TRU) and the Track Trigger Transmitter (TTT).

### Trigger Logic Unit (TRU)

The TRU has to select the fired pixel information from the matrix, which are in-time with the triggers sent by the Belle II system. In more details, this module employs two stages of memory in order to manage the data coming from the pixel matrix (Figure 3.17). These components are design in order to minimize power dissipation and to optimize the efficiency even in severe operating conditions: maximum hit rate of  $120 \text{ MHz cm}^{-2}$ , 30 KHz of trigger rate and  $10 \mu\text{s}$  of trigger delay.

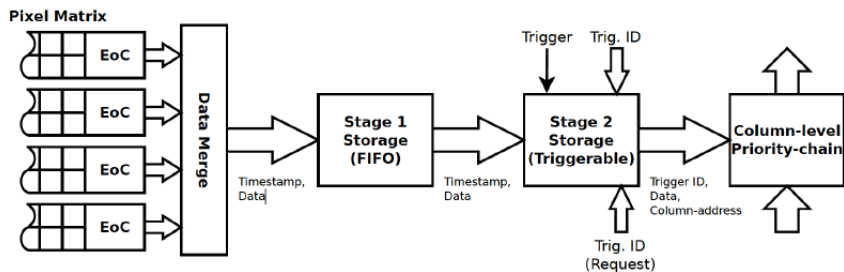


Figure 3.17: Schematic of the Trigger Logic Unit.

The first stage has to store the pixel information during the trigger delay ( $10 \mu\text{s}$ ). The second memory instead, has the task to compare the BCID of the fired pixel with each trigger time information buffered in a dedicated global memory which keeps track of received triggers. When they have a match, the pixel data is transferred to the Transmission Unit (TXU). Considering the BCID precision time, the time integration of the OBELIX sensor becomes 100 ns.

### Track Trigger Transmitter (TTT)

The TTT module divides the matrix in 8 logic regions (this value is still under study) and generates a one-byte word depending on the region that is fired. It is expected taht this information could be transmitted to trigger system within 100 ns and along a line of transmission parallel to the main data output of the sensor. This component behaviour is still under study and it needs of further simulations in correlation with the whole VTX system.

### Control Unit (CRU) and power dissipation

The OBELIX sensor, as well as TJ-Monopix 2, is configured by several registers which allow to set crucial features for its operation like threshold settings,

masked pixels, time response of the pixel and so on but also define its power consumption. The Control Unit is responsible for receiving these instructions about the configuration and the trigger information and at the same time sending out data coming from TXU module.

For what concern power dissipation, there are three main features which have the greatest impact: the biasing current flowing into the in-pixel amplifier (i.e.  $I_{BIAS}$ ), the BCID clock frequency (on which depends the timestamping precision) and the hit rate. In Figure 3.18 is shown the estimations of power dissipation as these parameters vary.

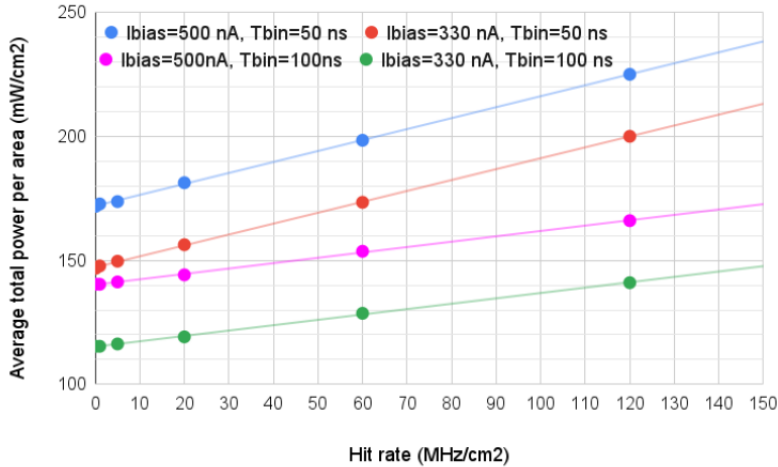


Figure 3.18: OBELIX sensor power dissipation depending on the front end current ( $I_{bias}$ , the BCID frequency (**tbin**) and the hit rate).

As we can see, the power consumption at the maximum hit rate of 120  $\text{MHz cm}^{-2}$  exceeds by little more than 10% the power budget of 200  $\text{mW cm}^{-2}$  considering the higher precision for the timestamp of 50 ns. Therefore to stay within the power budget it is necessary to find a compromise: reducing timing precision by worsening the BCID precision to 100 ns or decreasing the pre-amplifier biasing current causing a degradation of the time walk.

The first version of the sensor, called OBELIX-1, is being designed and the submission for fabrication is planned in the last month of 2023. A second improved version, OBELIX-2, will be designed based on performance studies on the first version and it is expected that it will be the final sensor needed for the experiment.

## 4. Conclusions

# List of Figures

1.1	Particle classification in the Standard Model.	4
1.2	Example of the kinematics of the golden channel of Belle II experiment.	6
1.3	SuperKEKB accelerator structure.	8
1.4	Comparison between the beam schemes used in KEKB and SuperKEKB.	9
1.5	Belle II detector.	10
1.6	A schematic view of the Belle II vertex detector with a Be beam pipe and the six layers of PXD and SVD.	11
1.7	Schematic view of the CDC drift cells: blue dots represent the axial wires and the pink empty ones the stereo wires.	11
1.8	TOP detector.	12
1.9	ARICH detector.	12
1.10	Summary of the main characteristics of all subdetectors.	13
1.11	Total recorded integrated luminosity before Long Shutdown 1.	14
1.12	Luminosity projection plot (plan for the coming years).	15
2.1	Measured Belle II background in June 2021. Each column shows different background sources for Belle II sub-detectors and also for superconducting quadrupole magnet (backward and forward) and the beam pipe.	18
2.2	Background rate limits for Belle II detector sub-systems. The third column shows the total measured background rate in June 2021.	18
2.3	Schematic of DuTiP circuits.	22
2.4	The size of Small (S) and Large (L) DuTiP chips.	23
2.5	DuTiP prototypes.	24
2.6	Overall VTX layout.	24
3.1	Concept of VTX layout with 5 barrel layers, filling the current VXD volume.	26
3.2	Sketch of the all-silicon ladder concept of the iVTX. Four dummy sensors are shown in blue on the silicon support in grey. The yellowish lines instead, indicate power and data transmission lines. Power is delivered to the ladder by a flex cable, which also transmits data to and from the chips in the final one.	27
3.3	Eye diagrams of the iVTX data transmission lines at four different locations on the ladder.	28

3.4	Prototype of the layer 5, called <i>truss</i> , which is the longest, made from thin carbon fibre structures. . . . .	29
3.5	A prototype of the cold-plate for cooling. One coolant tube(golden) is connected to the cold plate(black) and turns 180° on the other end (not shown) so that the coolant flows in both directions and thus leaves on the same side it starts. . . . .	29
3.6	Schematic view of possible solutions for the three outermost layers. . . . .	30
3.7	An exploding drawing of a fully assembled layer 5 ladder. . . . .	30
3.8	Eye diagram for the oVTX transmission line signal integrity of the layer 5 flex cable. . . . .	31
3.9	Reconstruction efficiency and purity for the the decay chain $B^0 \rightarrow D^{*-} l^+ \nu$ , with $D^{*-} \rightarrow \bar{D}^0 \pi_{soft}^-$ and $\bar{D}^0 \rightarrow K^+ \pi^-$ , for the nominal Belle II detector at the intermediate background conditions ( <b>v2</b> ) and the nominal configuration of VTX in all three background scenarios. . . . .	33
3.10	Reconstruction efficiency of $B^0 \rightarrow D^{*-} l^+ \nu$ as a function of the transverse momentum of the $\pi_{soft}^-$ (from $D^{*-} \rightarrow \bar{D}^0 \pi_{soft}^-$ ) in the plot on the left and of the polar angle of the $\pi_{soft}^-$ on the right. The shaded blue histograms represents the momentum spectrum of the $\pi_{soft}^-$ . The nominal Belle II geometry efficiency in the intermediate background scenario ( <b>v2</b> ) is represents by black dots and it is compared with the nominal VTX configuration in the optimistic ( <b>v1</b> , green squares), medium ( <b>v2</b> , blue upward pointing triangles) and pessimistic ( <b>v3</b> , red downward pointing triangles) background hypotheses. The bottom plots show the ration between nominal Belle II and nominal VTX in the <b>v2</b> background scenario. . . . .	33
3.11	On the left: comparison of the B decay vertex resolution along the $z$ axis in $B^0 \rightarrow J/\psi K_S^0$ events for the nominal Belle II (solid line), nominal VTX (dotted line) and alternative VTX geometry (filled grey histogram). The bottom plot shows the ratio between the VTX geometries (empty squares the nominal one and filled triangles the alternative) and nominal Belle II. On the right: B decay vertex resolution along the $z$ axis for the nominal VTX geometry in the three background scenarios: optimistic <b>v1</b> (green solid line), intermediate <b>v2</b> (blue dotted line) and pessimistic <b>v3</b> (red filled histogram). The bottom plot represents the ratio between the two higher background scenarios and the optimistic one. . . . .	34
3.12	$B_{sig}$ vertex resolution along the $z$ axis for the three detector layouts and the three background scenarios. . . . .	35

3.13	On the left: comparison of the $K_S^0$ decay vertex resolution along the $z$ axis in $B^0 \rightarrow J/\psi K_S^0$ events for the nominal Belle II (solid line), nominal VTX (dotted line) and alternative VTX (filled grey histogram). The bottom plot shows the ratio between the VTX geometries (empty squares for the nominal and filled triangles for the alternative) and nominal Belle II detector. On the right: $K_S^0$ decay vertex resolution along the $z$ axis for the nominal VTX in the three background scenarios: optimistic <b>v1</b> (green solid line), intermediate <b>v2</b> (blue dotted line) and pessimistic <b>v3</b> (red filled histogram). The bottom plot represents the ratio between the two higher background scenarios and the optimistic one. . . . .	35
3.14	OBELIX chip design. . . . .	36
3.15	Designed features of the OBELIX sensor. . . . .	37
3.16	Comparison between OBELIX requirements and TJ-Monopix 2 features. . . . .	37
3.17	Schematic of the Trigger Logic Unit. . . . .	38
3.18	OBELIX sensor power dissipation depending on the front edn current ( $I_{bias}$ , the BCID frequency ( <b>tbin</b> ) and the hit rate). . . . .	39

## List of Tables